INTERACTIONS BETWEEN CARBON STEEL AND UO_2 CORROSION FRONTS INSIDE A FAILED NUCLEAR WASTE CONTAINER

Shannon L.W. Hill[1], Nazhen Liu[1], Ziqiang Qin[1], Dmitrij Zagidulin[1], and David W. Shoesmith[1,2]

[1]Western University, 1151 Richmond Street, London, ON., N6A 5B7, Canada

[2]Surface Science Western, 999 Collip Circle, London, ON., N6G 0J3, Canada

ABSTRACT

The corrosion of carbon steel in the chloride-dominated groundwaters anticipated inside a failed spent fuel waste container has been studied in the presence of small concentrations of added hydrogen peroxide. Solutions with peroxide concentrations in the micro-molar range were found to accelerate steel corrosion slightly leading to the formation of Fe^{III}-containing corrosion product deposits but not to passivation of the steel. Calculations using a model for fuel and steel corrosion inside a failed waste container show that peroxide concentrations at the steel surface should be many orders of magnitude less than these micro-molar levels. It can be concluded that the redox scavengers, $Fe^{2+}$and H_2, produced by the active corrosion of the steel, will be available to suppress the radiolytic corrosion of the fuel and to avoid the associated radionuclide release processes.

Keywords: steel corrosion, nuclear waste containers, radiolytic spent fuel corrosion.

1. INTRODUCTION

A by-product of the use of nuclear energy is the generation of spent fuel. As of 2014 roughly 2.51 million bundles of used CANDU fuel are being stored at reactor sites[1]. In Canada the plan is to seal the spent nuclear fuel in metallic containers and emplace them in a deep geologic repository (DGR)[2]. This approach is based on multiple barriers with the primary barrier being a carbon steel vessel with an outer corrosion resistant Cu coating[3]. While copper is thermodynamically stable under anoxic conditions and should undergo minimal corrosion[4][5], the consequences of container failure must be considered.

Within a failed container, two corrosion fronts will be established, one on the fuel surface and a second on the inner surface of the steel vessel (Figure 1). While the groundwaters entering the container will be anoxic, radioactive decay processes in the fuel will cause water radiolysis with the radiolytic oxidants leading to fuel corrosion[6]. The dominant oxidant will be H_2O_2 due to alpha-radiolysis[7–9]. The H_2O_2 can either cause fuel corrosion, decompose, or be transported away from the surface.

The second corrosion front on the surface of the steel will lead to the production of soluble Fe^{2+} and H_2 as well as a surface layer of magnetite (which is not expected to passivate the steel). The model recently developed by Wu et al.[9] shows that corrosion of the fuel will be strongly influenced by the interaction of radiolytic oxidants with the products of steel corrosion. The Fe^{2+} will react with the radiolytic H_2O_2 via the Fenton reaction

$$2Fe^{2+} + H_2O_2 \rightarrow 2Fe^{3+} + 2OH^- \quad (1)$$

with model calculations indicating that [Fe^{2+}] in the range 0.1 µM to 1.0 µM will consume 67% to 90% of the radiolytic H_2O_2. However, the dominant species controlling fuel corrosion was found to be H_2 which calculations suggested could completely suppress fuel corrosion when present at µM levels.

For Fe^{2+} and H_2 to control redox conditions inside a failed container it is imperative that the steel vessel remain in the active condition. A possible mechanism by which the steel could be passivated and Fe^{2+}/H_2 production suppressed, is passivation of the steel by reaction with radiolytic H_2O_2 transported via the

groundwater in the container. Here, we investigate the corrosion of carbon steel in H_2O_2-containing solutions under both deaerated conditions, when traces of dissolved O_2 could be present in the solution, and under anaerobic conditions when dissolved O_2 levels would be expected to be ~0.1 ppb. The results of this study are then compared to model calculations, to assess whether or not steel passivation is a possibility.

2. EXPERIMENTAL

2.1 Materials and Electrode Preparations

Electrodes were fabricated using A516 Gr 70 carbon steel (0.23 C; 1.11 Mn; 0.07 P; 0.10 S; 0.26 Si; 0.01 Cu; 0.01 Ni; 0.02 Cr; 0.004 Mo; 0.036 Al; 0.019 V; 0.003 O [wt%], balance Fe). For the experiment performed under deaerated conditions on the bench-top, the electrode was a rectangular rod 6.5 cm in length with a 1 cm height and width. For the experiment performed in an anaerobic chamber, the electrode was a circular coupon (1.0 cm diameter) emplaced in a high-performance epoxy resin with a single exposed flat face (0.7854 cm^2). The connection between the electrode and the stainless steel rod used to connect the electrode to external measuring circuits was covered first with laboratory film (Parafilm), and then with several layers of Teflon tape to prevent exposure of the connection to the electrolyte. The electrodes were wet polished with a series of SiC papers (Presi) to a final 1200 grit finish and rinsed in ultra-high purity water (conductivity of 18.2 MΩ•cm) before emplacement either directly into the electrolyte solution or into an anaerobic chamber in preparation for electrolyte exposure.

2.2 Electrochemical Cell and Equipment

Experiments were conducted in a three-compartment glass electrochemical cell equipped with a Pt counter electrode and a saturated calomel reference electrode (SCE; 0.241 V vs. SHE). All potentials are reported on the SCE scale. In the deaerated bench-top experiment, the cell was housed within a grounded Faraday cage to minimize interference from external noise. For the anaerobic experiment, the cell was placed in an anaerobic chamber to avoid the influx of atmospheric O_2. For the deaerated bench-top experiment a Solartron 1480 multistat running Corrware software was used to control applied potentials and to record current responses. For the experiment performed in the anaerobic chamber a Solartron Analytical Modulab was used with raw data converted and analyzed using Corrware software.

2.3 Experimental Solutions

Experiments were performed in a solution containing 0.1 M NaCl, 0.1 M Na_2SO_4 and 0.01 M $NaHCO_3/Na_2CO_3$ set to a pH of 8.9 ± 0.5 (i.e., within the pH range of 7-10 expected for groundwaters). In the bench-top deaerated experiment, the solution was continuously purged with UHP Ar beginning one hour prior to measurements. In the anaerobic chamber experiment, ultra-high purity water was purged with UHP Ar at a high flow rate for one hour prior to being sealed and transferred into the anaerobic chamber. The flask was sealed with the entire volume of the flask filled with water to avoid trapped air. Once inside the chamber no additional Ar purging was necessary.

2.4 Experimental Procedure

Electrodes were cathodically cleaned at a potential of -1.3 V for three minutes to reduce air-formed surface oxides. The potential was then held at -1.1 V to avoid further H_2 production while H_2 bubbles were removed from the surface. Throughout an experiment the corrosion potential (E_{CORR}) was monitored continuously and linear polarization resistance (LPR) measurements made every 3 to 6 hours for the deaerated and anaerobic cases. LPR measurements were performed by scanning the potential ± 10 mV from the E_{CORR} at a scan rate of 0.1667 mV/s, with each measurement requiring a total of 4 or 5.8 min, respectively.

2.5 Surface Analysis

To identify the iron corrosion products formed, a Renishaw 2000 Raman spectrometer with a 632.8 nm laser line, using an optical microscope with a 50X magnification objective lens, running GRAMS 386 software was used. To identify the film morphology, SEM was performed using a Hitatchi S-4500 Field Emission SEM for the deaerated experiment and a LEO (Zeiss) 1540XB FIB/SEM for the anaerobic experiment.

2.6 Computational Modelling

The mathematical model is numerically solved using COMSOL Multiphysics (version 4.3.1.151, COMSOL Inc.) a commercial simulation package based on the finite element model. The model was simulated using the diluted species transportation module of the COMSOL software.

3. RESULTS AND DISCUSSION

3.1 Electrochemical Analysis

Figure 2 and 3 show the E_{CORR} and polarization resistance (R_P) values recorded under deaerated and anaerobic exposure conditions over periods of 35 and 66 days, respectively. Small additions of H_2O_2 were made periodically. The red points indicate the LPR measurements made immediately after an addition. In both experiments, the value of E_{CORR} is < -800 mV prior to H_2O_2 addition confirming that corrosion is proceeding under anoxic conditions by reaction of the steel with water. Under these conditions, the steel would be expected to form a magnetite layer

$$3Fe + 4H_2O \rightarrow Fe_3O_4 + 4H_2 \quad (2)$$

accompanied by dissolution as Fe^{2+}, the latter being a process accelerated by the anion content of the solution, for example HCO_3^-/CO_3^{2-} which is known to form soluble complexes such as $FeHCO_3^+$, $Fe(CO_3)_2^{2-}$, and $Fe(HCO_3)_2$. The increases in R_P values in both environments are consistent with the thickening of a surface Fe_3O_4. This initial film growth appears to occur slightly differently in the two experiments, the R_P value increasing to a substantially higher value in the anaerobic compared to the deaerated solution (Figure 2 and 3). However, even prior to the addition of H_2O_2, R_P begins to decrease again in the anaerobic experiment, Figure 3. This may indicate the initially formed Fe_3O_4 film is restructured, possibly developing some porosity.

On first adding H_2O_2 (at (1) in both experiments, Figure 2 and 3) the E_{CORR} responds but only transitorily, eventually recovering to the value prior to the addition. This response is seen as positive-going spikes in the potential, and is more noticeable for the anaerobic experiment (Figure 3). Minor changes in R_P are also observed but are less readily discernible. Further additions of H_2O_2 to the deaerated experiment (indicated by the red points in Figure 2) again show only transitory changes in E_{CORR} but also temporary decreases in R_P confirming the surface is reactive in the presence of H_2O_2. Increasing $[H_2O_2]$ to 5.2 μM after 10 days ((2) in Figure 2) lead to a significant increase in R_P but only a small decrease in E_{CORR}. The most likely reason for the increase in R_P is an accelerated growth of Fe_3O_4 surface layer or a decrease in its porosity. On increasing the $[H_2O_2]$ to ≥6.1 μM ((3) in Figure 2) the E_{CORR} begins to increase slightly accompanied by successive decreases in R_P as the $[H_2O_2]$ is increased. Figure 4(a) shows that metastable transients occur during this period as R_P decreases. The positive surge in E_{CORR} followed by a slower recovery to the original value would be consistent with enhanced anodic dissolution occurring at fracture sites in the surface film followed by their subsequent repair as the film is either reformed or corrosion product is deposited within the breakdown site. Whether or not steel corrosion is accompanied by H_2O_2 decomposition

$$2H_2O_2 \rightarrow O_2 + 2H_2O \quad (3)$$

as might be expected on a conductive and probably catalytic Fe_3O_4 surface, cannot be discerned in these experiments.

After 22 days at an added $[H_2O_2]$ of 16.1µM ((4) in Figure 2) the slight increase in E_{CORR} is accompanied by a doubling of R_P. This is rapidly followed by a major and irreversible transition in E_{CORR} to a value in the region of -550 mV. This transition is accompanied by a substantial decrease in R_P. During and after this transition R_P becomes erratic and no longer a reliable indication of the corrosion rate. Similar coincidental behaviour in E_{CORR} and R_P on carbon steel has been observed previously under similar deaerated conditions[10,11]. The increase in R_P during the early stages of the transition can be interpreted as an attempt by the steel to passivate and the subsequent decrease as the transition progresses to completion to the formation of localized corrosion sites; i.e., pitting. Under these conditions the R_P values reflect the presence of these actively corroding locations and are no longer a reliable indication of the general corrosion behaviour of the steel.

Despite the considerably higher R_P values the steel electrode exposed in the anaerobic experiment shows a similar decrease in R_P without any significant increase in E_{CORR}, as the $[H_2O_2]$ is increased, Figure 3 (12 to 30 days). However, further increases in $[H_2O_2]$ to a final concentration of 6.0µM ((5) in Figure 3) did not stimulate the transition observed in the deaerated experiment, with E_{CORR} achieving a steady-state value of ~ -800 mV after 65 days.

Based on a comparison of the two experiments and previous observations, the transition to a passive state undergoing localized corrosion observed in the deaerated experiment can be attributed to the slow passivation of the steel surface caused by the low background concentration of dissolved O_2 present in this experiment. The alternative source of O_2, H_2O_2 decomposition by reaction 3, is present in both experiments, but apparently not in sufficient quantities to induce passivation.

3.2 Surface Analysis of Steel in the Deaerated Solution

Figure 5 shows the SEM micrographs recorded on the steel surface after the 35 day exposure to the deaerated solution. The low magnification micrograph (Figure 5(a)) shows that the surface is covered with a uniformly distributed compact film with areas apparently covered with a thin deposit. A number of individual larger crystals (or deposits) are also visible. The compact film is thin enough, the polishing lines of the initially prepared steel still being discernable. Figure 5(b) shows that the thin deposit is comprised of hexagonal crystals grown at fractures/faults in the compact layer. This morphology is consistent with the observation of potential transients, Figure 4(a), indicating periodic breakdown of the compact layer followed by their repair due to the subsequent deposition of corrosion product. Several well-formed hexagonal crystals (Figure 5(c)), on the order of 5-15 µm in size, were also dispersed over the sample surface.

Figure 6 shows the ex-situ Raman analyses for both the general surface regions and the large hexagonal crystals (Figure 5(c)). Spectra (a) and (b) recorded on the general surface indicate the presence of green rust (GR) which is a frequently observed corrosion product on iron surfaces when traces of dissolved O_2 are present[12] as would be the case in the deaerated experiment. GRs are layered double-hydroxide (LDH) compounds isostructural to pyroaurite ($Mg_6Fe_2(OH)_{16}CO_3$) consisting of hcp sheets of $Fe^{(II)}(OH)_6$ octahedra where some $Fe^{(II)}$ has been replaced by $Fe^{(III)}$. The substitution of $Fe^{(III)}$ into the layers lends a positive charge to the structure which is then balanced by anions located between the $Fe(OH)_2$ sheets[13–15]. The most commonly found anions within the GR structure are chloride (green rust I) and sulphate (green rust II). The small bands, Figure 6(a) and 6(b), from ca. 200-250 cm^{-1} (ref. 219-221 cm^{-1})[16] suggest that the coordinating anion of the green rust formed in this deaerated experiment chloride rather than carbonate or sulphate, indicating an idealised structure for the GR(Cl^-) of $[Fe_3^{(II)}Fe^{(III)}(OH)_8][Cl{\bullet}2H_2O]$[17,18]. The bands at 433 and 516 cm^{-1} (ref. 434 and 510 cm^{-1})[16] are assigned to the Fe^{2+}—OH and Fe^{3+}—OH stretching modes of the green rust structure[16]. From the

Raman data, the hexagonal plates seen within figure 5(b) can be assigned to the GR(Cl^-) corrosion product. Several others have also reported GR to have a hexagonal platelet structure[12,19].

Raman analysis of the large hexagonal crystals (line 6(c)) seen in Figure 5(c) suggests they are composed of ferrihydrite based on Raman bands at 359, 512 and 706 cm^{-1} (ref. 370, 510 and 710 cm^{-1})[20]. The band centered at 1370 cm^{-1} (ref. 1340 cm^{-1}) may originate from the ferrihydrite as observed by Mazzetti and Thistlethwaite[20]. Two forms of ferrihydrite are reported, 2-line and 6-line, so named because their XRD patterns show 2 or 6-8 reflections as the structural order increases[12]. The lack of asymmetry in the peak at 706 cm^{-1} and the greater intensity of the band at 359 cm^{-1} to that of the 512 cm^{-1} suggests that the form of ferrihydrite formed during the corrosion process was the 6-line form[20]. The structure seen within Figure 5(c) for the SEM micrograph showing a highly ordered hexagonal crystal is also in line with the formation of a more structurally ordered ferrihydrite. Ferrihydrite ($Fe_{10}O_4(OH)_2$) has been shown to form in atmospheric corrosion conditions[21,22] and is a metastable precursor to phases such as hematite (α-Fe_2O_3).

The absence of a Raman signal for Fe_3O_4 (expected at 667 cm^{-1}) is at first surprising since one would have expected the compact film to be dominantly this phase. This suggests either the compact film is amorphous or has been converted to GR by H_2O_2 or the traces of dissolved O_2 present in this experiment. This latter explanation would support our conclusion that the general surface is at least partially passivated as indicated by the major transition in E_{CORR}, Figure 2.

3.3 Surface Analysis of Steel in the Anaerobic Solution

Figure 7 shows the SEM micrographs recorded on the steel surface after 66 days of exposure within the anaerobic experiment. The film appears to be thin and compact as evidenced by the visible polishing lines (Figure 7(a)). The cracking of the film was likely induced by the vacuum exposure of both the anaerobic chamber and that of the SEM itself. Figure 7(b) shows that the film is composed of a fine crystalline film interspersed with smooth hexagonal crystals. One small region of the surface was shown to be covered in a thicker and highly irregularly shaped crystalline corrosion product (Figure 7(c)).

Figure 8 shows the ex situ Raman spectra recorded at several locations across the surface. The band at 667 cm^{-1} (ref. 667 cm^{-1})[23] in line (a) is assigned to the strongest A_{1g} mode of Fe_3O_4[23]. Formation of Fe_3O_4 confirms the anoxic corrosion of the steel under anaerobic conditions. Two bands centered between 1300 and 1600 cm^{-1} within line (a) are attributed to Fe_3C residues left behind from the dissolution of the α-Fe in the pearlite grain structure of the steel[23]. Evidence of Fe_3C residues of pearlite indicates the presence of areas covered only by a thin Fe_3O_4 film, which would further suggest that the surface of the steel coupon has not been passivated by the addition of the H_2O_2. The large fluorescence in the spectrum, Figure 8(a), is due to electronic excitations of the underlying Fe metal[11].

Spectra (b) and (c) show bands at 330, 420 and 730 cm^{-1} which could indicate the formation of either akaganeite (β-$FeO(OH)_{1-x}Cl_x$)[24] which is known to form under chloride containing aqueous conditions[25,26], or maghemite (ref. 350, 505, 660 and 710 cm^{-1})[27]. Réguer et al. reported strong Raman bands at 310, 390, and 720 cm^{-1} in conjunction with less intense bands at 490, 540, and 610 cm^{-1} for akaganeite[26]. Rémazeilles et al. reported broad bands at 308, 390, 418 and 722 cm^{-1}[25]. The large discrepancy in the assignment of Raman bands for β-FeOOH may be due to the various chloride contents possible within the structure which have been shown to alter the Raman spectra[26]. The absence of the distinct peak at 310 cm^{-1} for akaganeite and the band at 660 cm^{-1} for maghemite makes the structure elucidation precarious. All iron oxides present a main peak in the region of 650-700 cm^{-1}, except in the case of hematite, goethite, and lepidocrocite[27]. As such, the classification of many iron oxides requires examination of the shape and broadness of the peaks in this region. In our case, the breadth of the peak in this region, as well as the relatively low intensity of the spectrum makes it hard to definitively state its compositions. There is good possibility that spectra (b) and (c) may be caused either by a very poorly crystalline iron species or a mixture of several iron oxide/oxyhydroxide species.

The Raman band at 1072 cm^{-1} (ref.1070-1072 cm^{-1}, Figure 8(d)) is due to the v_1 C—O symmetric stretching of a coordinated CO_3^{2-} species[28,29]. However, the lack of any other Raman bands in the spectrum suggests that while the CO_3^{2-} component of the film is seen, the remainder of the corrosion product structure is not Raman active. The highly crystalline morphology seen in the SEM micrograph, Figure 8(c), is similar to that seen in our own work (unpublished), on specimens not exposed to H_2O_2, which also displayed the characteristic C—O stretching Raman band at 1072 cm^{-1}. FTIR analysis of these samples confirmed the formation of chukanovite ($Fe_2(OH)_2CO_3$). Pandarinathan et al. also showed the same structural morphology for chukanovite formed during the corrosion of sand-deposited carbon steel in CO_2 saturated brines at 80°C[30].

3.4 Computational Modelling

A model developed previously to determine fuel corrosion rates[9] was adapted to include the possibility of the reaction of H_2O_2 with the inner surface of the steel vessel. This model takes into account the consumption of H_2O_2 by the corrosion of the fuel, decomposition catalyzed by the fuel surface, and by reaction with soluble $Fe^{2+}$from the corroding steel vessel in the Fenton reaction (reaction 1). The expected long term corrosion rate of the steel is expected to be around 0.1 μm/yr[31] with corrosion proceeding on a magnetite-covered surface. The model was used to investigate the [H_2O_2] expected on the inside surface of the steel container.

Figure 9(a) shows the [H_2O_2] profile between the fuel surface, at which it is produced (0 mm on the plot), and the steel surface set at a distance of 1 mm from the fuel surface. Such a separation is conservatively close and minimizes the transport range for H_2O_2 between the two surfaces. After 500s the [H_2O_2] at the fuel surface is calculated to be 4.05 x 10^{-10} M. Figure 9(b) shows that the [H_2O_2] at the steel surface becomes negligibly small after ~8000s of radiolytic H_2O_2 production at the fuel surface. The variability in calculated values is due to the “noise” encountered in the numerical calculations at such low values.

Since the corrosion rate of the steel is uncertain, the sensitivity of the model to various parameters and reactions was evaluated. As expected, increasing the distance between the fuel and steel surfaces to more realistic separations leads to a decrease in [H_2O_2] at the steel surface. Figure 10 shows the influence of steel corrosion rate on the predicted [H_2O_2] at the steel surface. An increase in corrosion rate from 0.1 μm/yr to 1.0 μm/yr leads to a decrease in this concentration. This can be attributed to the increase in [Fe^{2+}] and [H_2] both of which increase the consumption rate of H_2O_2. For H_2 this is by reaction with H_2O_2 catalyzed on the noble metal particles in the spent fuel and for Fe^{2+} by reaction with H_2O_2 in the Fenton reaction. Additional calculations show that the key reaction consuming H_2O_2 and preventing its transport to the steel surface is the Fenton reaction (reaction 1). For the [H_2O_2] at the steel surface to approach the micro-molar level this reaction would have to not occur, which is extremely unlikely.

Based on these calculations we can conclude that it is highly unlikely that H_2O_2 concentrations will reach the micro-molar levels at which an influence on steel corrosion would become significant, which, as discussed above, would be in the 1 to 10 μM range. Even for concentrations in this range there is no experimental indication that exposure to H_2O_2 would lead to passivation of the steel and suppression of the redox scavengers, Fe^{2+} and H_2.

CONCLUSIONS

The influence of H_2O_2 on the corrosion of carbon steel has been investigated under deaerated conditions, when traces of dissolved O_2 could be present, and under anaerobic conditions, when the [O_2] would be expected to be at the ppb level.

Under anaerobic conditions active steel corrosion, producing $Fe^{2+}$and H_2 was maintained up to [H_2O_2] = 6 μM. For deaerated conditions, passivation leading to pitting occurred for added [H_2O_2] ≥ 10 to 15 μM. However, this was attributable to the presence of traces of dissolved O_2 despite the continuous Ar purge.

The presence of non-passivating Fe^{III}-containing corrosion products confirmed the interaction of H_2O_2 with the steel.

Model calculations indicate that $[H_2O_2] > 10^{-9}$M are effectively unachievable at the steel surface.

Based on these results it can be concluded that active steel corrosion will be maintained inside a failed waste container, and that the soluble corrosion products will be available to supress fuel corrosion and radionuclide release.

ACKNOWLEDGEMENTS

This research is funded through the joint support of the Canadian Natural Sciences and Engineering Research Council (NSERC) and the Nuclear Waste Management Organization (NWMO), Toronto, under an Industrial Research Chair agreement. We thank the UWO nanofabrication facility for the use of their SEM.

REFERENCES

[1] M. Garamszeghy, Nuclear Fuel Waste Projections in Canada - 2014 Update, 2014.
[2] J. McMurry, D.A. Dixon, J.D. Garroni, B.M. Ikeda, S. Stroes-Gascoyne, P. Baumgartner, et al., Evolution of a Canadian deep geologic repository: Base Scenario, Ontario Power Generation, 2003.
[3] P.G. Keech, P. Vo, S. Ramamurthy, J. Chen, R. Jacklin, D.W. Shoesmith, "Design and development of copper coatings for long term storage of used nuclear fuel," *Corros. Eng. Sci. Technol.* 49 (2014) 425–430.
[4] F. King, M. Kolar, "A numerical model for the corrosion of copper nuclear fuel waste containers," *Sci. Basis Nucl. Waste Manag. Xix*. 412 (1996) 555–562.
[5] F. King, M. Kolar, The Copper Container Corrosion Model Used in AECL's Second Case Study, Ontario Power Generation, 2000.
[6] L. Wu, D.W. Shoesmith, "An Electrochemical Study of H2O2 Oxidation and Decomposition on Simulated Nuclear Fuel (SIMFUEL)," *Electrochim. Acta*. 137 (2014) 83–90.
[7] D.W. Shoesmith, Used Fuel and Uranium Dioxide Dissolution Studies - A Review, 2007.
[8] D.W. Shoesmith, "Fuel corrosion processes under waste disposal conditions," *J. Nucl. Mater.* 282 (2000) 1–31.
[9] L.D. Wu, Z. Qin, D.W. Shoesmith, "An improved model for the corrosion of used nuclear fuel inside a failed waste container under permanent disposal conditions," *Corros. Sci.* 84 (2014) 85–95.
[10] B.W.. Sherar, P.G. Keech, D.W. Shoesmith, "Carbon steel corrosion under anaerobic-aerobic cycling conditions in near-neutral pH saline solutions - Part 1: Long term corrosion behaviour," *Corros. Sci.* 53 (2011) 3636–3642.
[11] B.W.A. Sherar, P.G. Keech, Z. Qin, F. King, D.W. Shoesmith, "Nominally Anaerobic Corrosion of Carbon Steel in Near-Neutral pH Saline Environments," *Corrosion*. 66 (2010) 0450011–04500111.
[12] R.M. Cornell, U. Schwertmann, The iron oxides : structure, properties, reactions, occurrences, and uses, 2nd, compl, Wiley-VCH, Weinheim, 2003.
[13] G.W. Brindley, D.L. Bish, A.L. Mackay, "Green Rust - Pyroaurite Type Structure," *Nature*. 263 (1976) 353.
[14] R.M. Taylor, R.M. Mckenzie, "The Influence of Aluminum on Iron-Oxides .6. The Formation of Fe(Ii)-Al(Iii) Hydroxy-Chlorides, Fe(Ii)-Al(Iii)Hydroxy-Sulfates, and Fe(Ii)-Al(Iii)Hydroxy-Carbonates as New Members of the Pyroaurite Group and Their Significance in Soils," *Clays Clay Miner.* 28 (1980) 179–187.

[15] P. Refait, J.M.R. Genin, "Mechanisms of oxidation of Ni(II)-Fe(II) hydroxides in chloride-containing aqueous media: role of the pyroaurite-type Ni-Fe hydroxychlorides," *Clay Miner.* 32 (1997) 597–613.
[16] S. Simard, M. Odziemkowski, D.E. Irish, L. Brossard, H. Menard, "In situ micro-Raman spectroscopy to investigate pitting corrosion product of 1024 mild steel in phosphate and bicarbonate solutions containing chloride and sulfate ions," *J. Appl. Electrochem.* 31 (2001) 913–920.
[17] P. Refait, M. Abdelmoula, J.M.R. Génin, "Mechanisms of formation and structure of green rust one in aqueous corrosion of iron in the presence of chloride ions," *Corros. Sci.* 40 (1998) 1547–1560.
[18] P. Refait, J.M.R. Genin, "The Oxidation of Ferrous Hydroxide in Chloride-Containing Aqueous-Media and Pourbaix Diagrams of Green Rust One," *Corros. Sci.* 34 (1993) 797–819.
[19] P. Refait, J.A. Bourdoiseau, M. Jeannin, D.D. Nguyen, A. Romaine, R. Sabot, "Electrochemical formation of carbonated corrosion products on carbon steel in deaerated solutions," *Electrochim. Acta*. 79 (2012) 210–217.
[20] L. Mazzetti, P.J. Thistlethwaite, "Raman spectra and thermal transformations of ferrihydrite and schwertmannite," *J. Raman Spectrosc.* 33 (2002) 104–111.
[21] J.L. Jambor, J.E. Dutrizac, "Occurrence and constitution of natural and synthetic ferrihydrite, a widespread iron oxyhydroxide," *Chem. Rev.* 98 (1998) 2549–2585.
[22] S. Music, M. Gotic, S. Popovic, "X-ray Diffraction and Fourier-Transform Infrared-Analysis of the Rust Formed by Corosion of Steel in Aqueous-Solutions," *J. Mater. Sci.* 28 (1993) 5744–5752.
[23] C.T. Lee, M.S. Odziemkowski, D.W. Shoesmith, "An in situ Raman-electrochemical investigation of carbon steel corrosion in Na2CO3/NaHCO3, Na2SO4, and NaCl solutions," *J. Electrochem. Soc.* 153 (2006) B33–B41.
[24] J. Monnier, D. Vantelon, S. Reguer, P. Dillmann, "X-ray absorption spectroscopy study of the various forms of phosphorus in ancient iron samples," *J. Anal. At. Spectrom.* 26 (2011) 885–891.
[25] C. Rémazeilles, P. Refait, "On the formation of β-FeOOH (akaganéite) in chloride-containing environments," *Corros. Sci.* 49 (2007) 844–857.
[26] S. Reguer, D. Neff, L. Bellot-Gurlet, P. Dillmann, "Deterioration of iron archaeological artefacts: micro-Raman investigation on Cl-containing corrosion products," *J. Raman Spectrosc.* 38 (2007) 389–397.
[27] N. Boucherit, a. Hugot-Le Goff, S. Joiret, "Raman studies of corrosion films grown on Fe and Fe-6Mo in pitting conditions," *Corros. Sci.* 32 (1991) 497–507.
[28] M. Saheb, D. Neff, L. Bellot-Gurlet, P. Dillmann, "Raman study of a deuterated iron hydroxycarbonate to assess long-term corrosion mechanisms in anoxic soils," *J. Raman Spectrosc.* 42 (2011) 1100–1108.
[29] R.L. Frost, M.C. Hales, B.J. Reddy, "Aurichalcite - An SEM and Raman spectroscopic study," *Polyhedron*. 26 (2007) 3291–3300.
[30] V. Pandarinathan, K. Lepková, W. van Bronswijk, "Chukanovite (Fe2(OH)2CO3) identified as a corrosion product at sand-deposited carbon steel in CO2-saturated brine," *Corros. Sci.* 85 (2014) 26–32.
[31] F. King, Corrosion of carbon steel under anaerobic conditions, Wettingen, Switzerland, 2008.

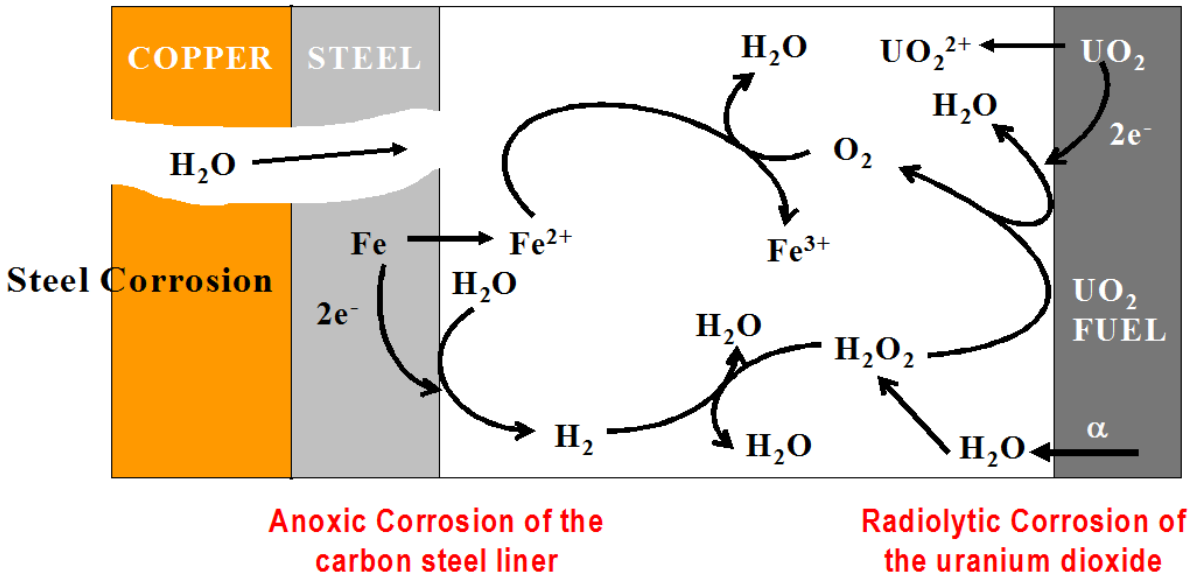

Figure 1. Interactions of the steel and UO_2 corrosion products and radiolytically produced oxidants within a failed spent nuclear fuel container.

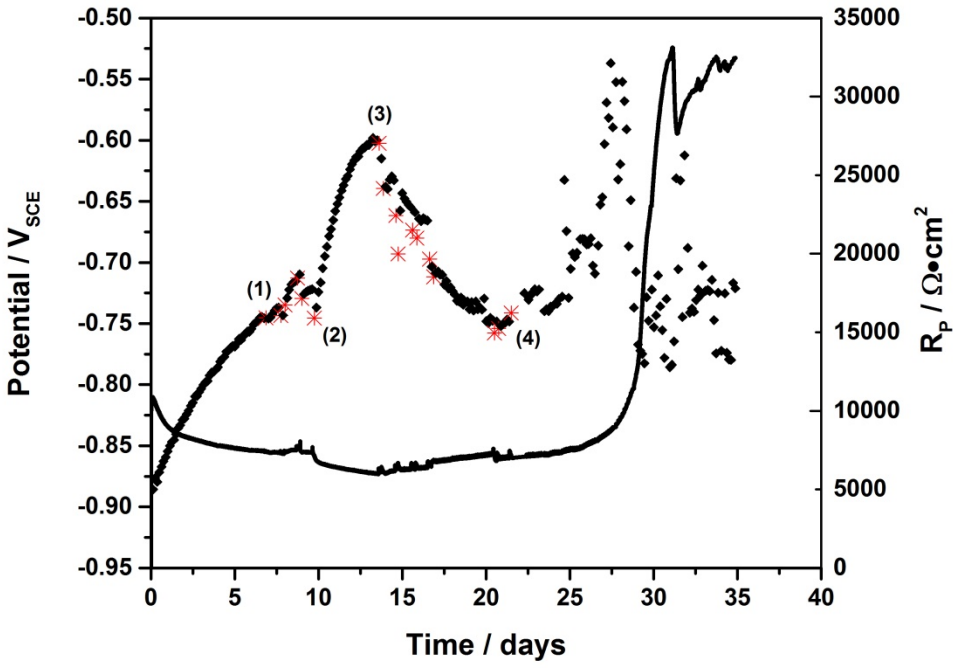

Figure 2. Corrosion potential (E_{CORR}) under deaerated conditions. Points indicate the R_P values, with the red points showing R_P values recorded after an addition of H_2O_2.

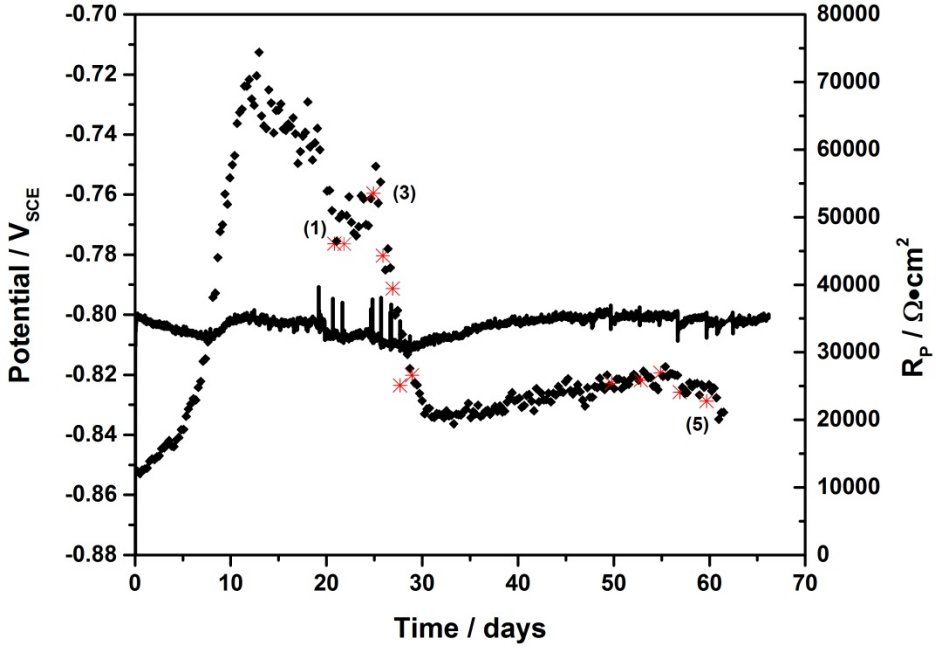

Figure 3. Corrosion potential (E_{CORR}) under anaerobic conditions ([O_2] ~ 0.1 ppb). Points indicate R_P values, with the red points showing R_P values recorded after the addition of H_2O_2.

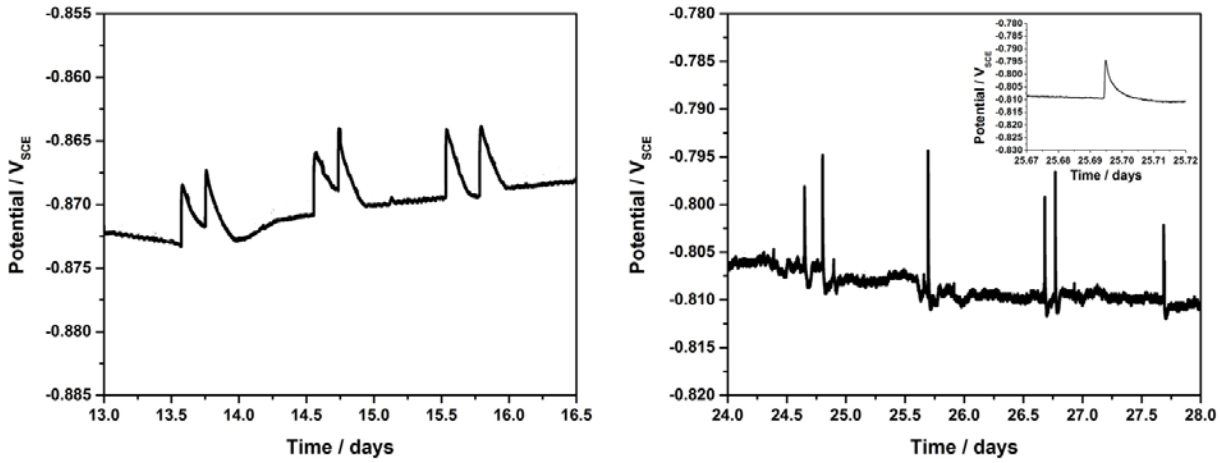

Figure 4. Metastable transients in E_{CORR} recorded under (a) deaerated and (b) anaerobic corrosion conditions.

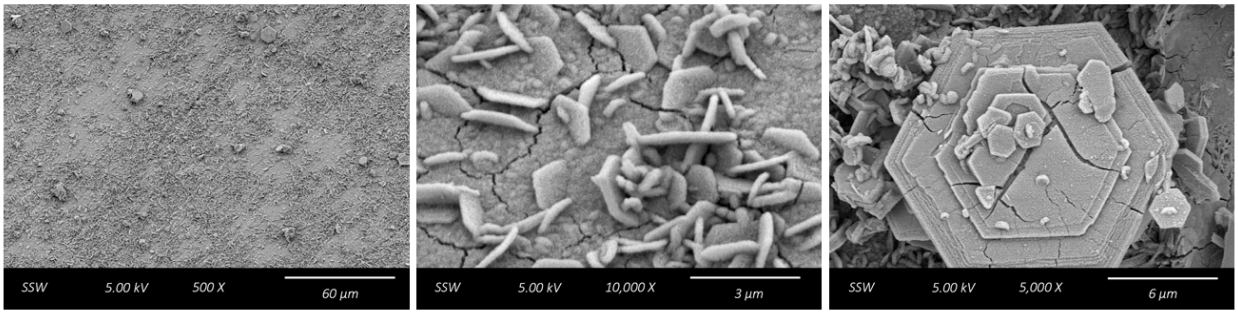

Figure 5. SEM micrographs showing the morphology of the corrosion film and deposits on the steel surface after corrosion under deaerated conditions.

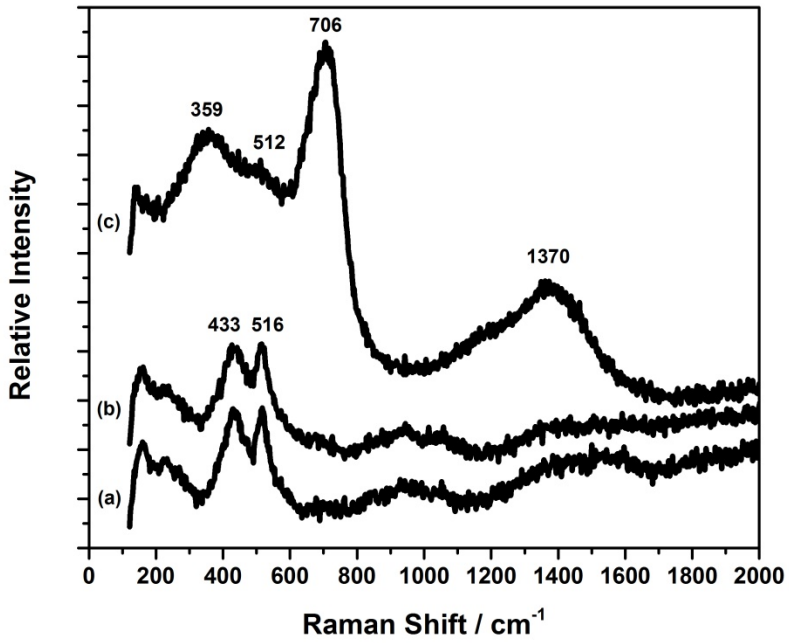

Figure 6. Raman spectra recorded on the steel after corrosion under deaerated conditions (Figure 2).

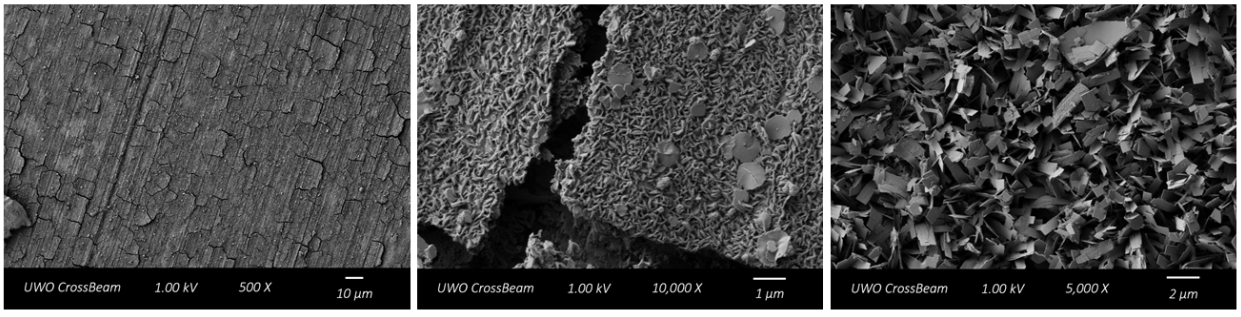

Figure 7. SEM micrographs showing the morphology of the corrosion film and deposits on the steel surface after corrosion under anaerobic conditions.

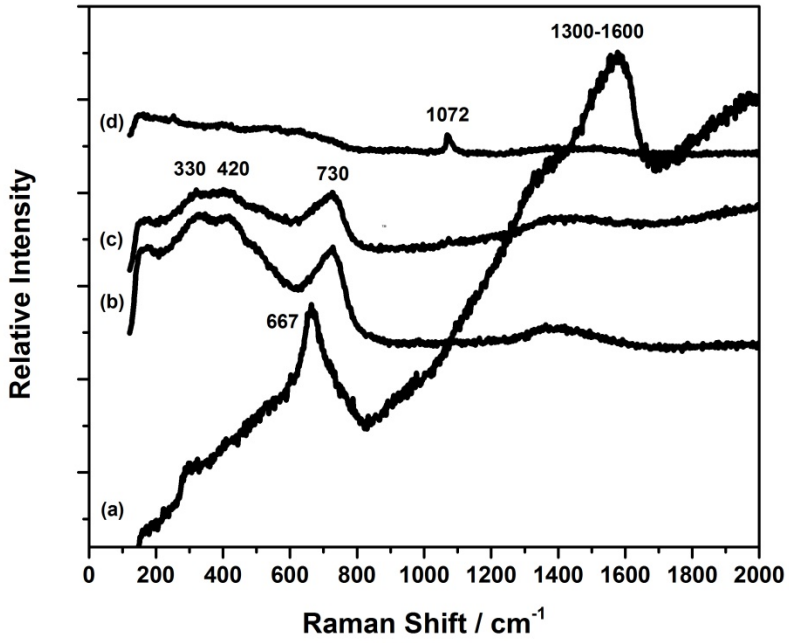

Figure 8. Raman spectra recorded on the steel after corrosion under anaerobic conditions (Figure 3).

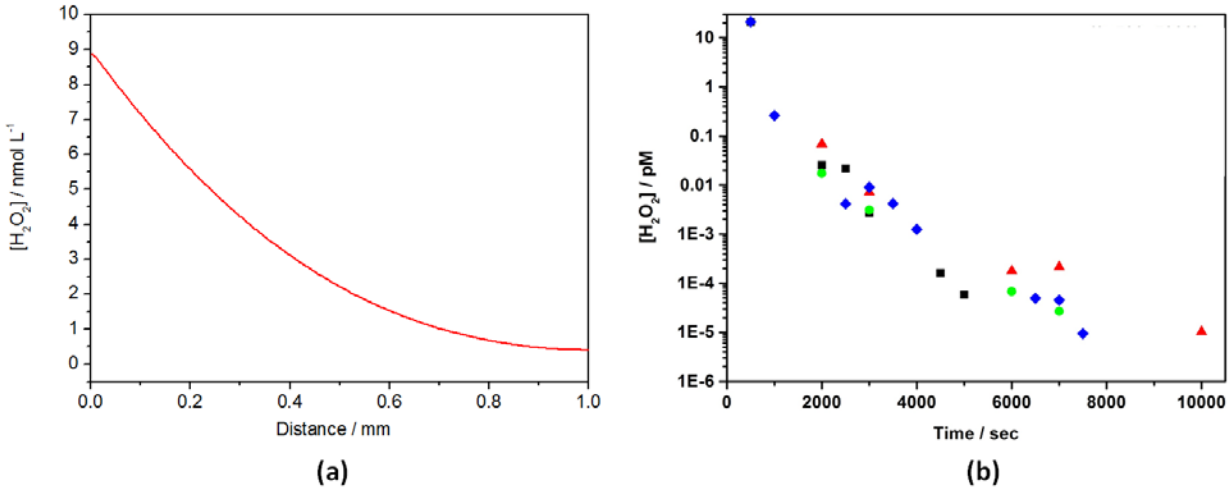

Figure 9: (a) $[H_2O_2]$ profile from the UO_2 surface (0.0 mm) to the surface of the carbon steel (1.0 mm) after 500s: (b) plot of $[H_2O_2]$ at the carbon steel surface as a function of the period of α-radiolysis at the fuel surface (surface separation, 1 mm).

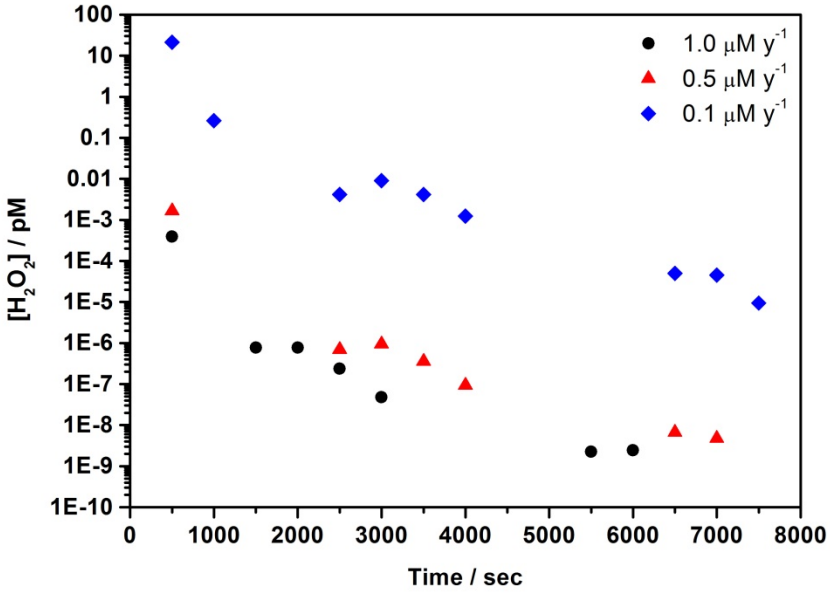

Figure 10: The influence of the steel corrosion rate on the $[H_2O_2]$ at the steel surface as a function of the period of α-radiolysis at the fuel surface (surface separation, 1 mm).